



Amorphous silica fiber matrix biomaterials: An analysis of material synthesis and characterization for tissue engineering

Hyun S. Kim^a, Sangamesh G. Kumbar^{a,b,c}, Syam P. Nukavarapu^{a,b,c,*}

^a Department of Biomedical Engineering, University of Connecticut, Storrs, CT, USA

^b Department of Material Science and Engineering, University of Connecticut, Storrs, CT, USA

^c Department of Orthopaedic Surgery, University of Connecticut Health, Farmington, CT, USA

ARTICLE INFO

Keywords:

Silica biomaterial
Porous matrix
ECM-Like fibrous structure
Biodegradable
Water absorption

ABSTRACT

Silica biomaterials including Bioglass offer great biocompatibility and bioactivity but fail to provide pore and degradation features needed for tissue engineering. Herein we report on the synthesis and characterization of novel amorphous silica fiber matrices to overcome these limitations. Amorphous silica fibers were fused by sintering to produce porous matrices. The effects of sacrificial polymer additives such as polyvinyl alcohol (PVA) and cellulose fibers (CF) on the sintering process were also studied. The resulting matrices formed between sintering temperatures of 1,350–1,550 °C retained their fiber structures. The matrices presented pores in the range of 50–200 μm while higher sintering temperatures resulted in increased pore diameter. PVA addition to silica significantly reduced the pore diameter and porosity compared with silica matrices with or without the addition of CF. The PVA additive morphologically appeared to fuse the silica fibers to a greater extent and resulted in significantly higher compressive modulus and strength than the rest of the matrices synthesized. These matrices lost roughly 30% of their original mass in an *in vitro* degradation study over 40 weeks. All matrices absorbed 500 wt% of water and did not change in their overall morphology, size, or shape with hydration. These fiber matrices supported human mesenchymal stem cell adhesion, proliferation, and mineralized matrix production. Amorphous silica fiber biomaterials/matrices reported here are biodegradable and porous and closely resemble the native extracellular matrix structure and water absorption capacity. Extending the methodology reported here to alter matrix properties may lead to a variety of tissue engineering, implant, and drug delivery applications.

1. Introduction

Bioglass is one of the widely accepted biomaterials of the 20th century [1–3]. Amorphous silica is the major constituent of Bioglass along with network-forming or modifying elements, such as calcium oxide (CaO) and phosphorous pentoxide (P₂O₅) [3]. Bioglass served as the first bioactive material, primarily due to its ability to form hydroxyapatite or bone mineral when exposed to simulated body fluids *in vitro* or implanted *in vivo* [4–6]. The major advantage of using Bioglass is its interaction with host tissue to promote bonding with soft as well as hard tissues [5,6]. Apatite mineral development on the surface of Bioglass has been explored extensively and occurs due to degradation and ionic interactions at the surface of the Bioglass [7–9]. Based on these properties, Bioglass-based products are clinically approved and currently used for

dental, craniofacial, and maxillofacial bone defect repair applications. However, due to the bulk nature of Bioglass and other melt-derived silica glasses, *in vivo* degradation of these biomaterials is limited and lacks porosity that would allow cell infiltration and *de novo* tissue formation [10,11]. These limitations present a major roadblock for their further adaptability and development in tissue engineering applications.

Among the several approaches to overcome Bioglass/silica-based biomaterial limitations are to use these biomaterials in the form of particulates for defect-filling applications. This allows space and gaps in between the particulates to serve as pores for cell infiltration [12]. However, such particulate systems are limited to non-load bearing applications due to lack of strength [12]. Significant development of sol-gel material processing allowed silica biomaterials with in-built porosity and pore structure [11]. The reported pores were in the

Peer review under responsibility of KeAi Communications Co., Ltd.

* Corresponding author. Department of Biomedical Engineering, University of Connecticut, Storrs, CT, USA.

E-mail address: syam.nukavarapu@uconn.edu (S.P. Nukavarapu).

<https://doi.org/10.1016/j.bioactmat.2022.04.002>

Received 11 January 2022; Received in revised form 9 March 2022; Accepted 2 April 2022

2452-199X/© 2022 The Authors. Publishing services by Elsevier B.V. on behalf of KeAi Communications Co. Ltd. This is an open access article under the CC BY-NC-ND license (<http://creativecommons.org/licenses/by-nc-nd/4.0/>).

nanometer range (10–1000 nm) and final products are often presented as nano- or microparticles and xerogel glasses [11]. However, the optimal pore size for tissue engineering is reported to be 50–300 μm to allow for cell infiltration and efficient nutrient transport and waste removal [13–15]. Other efforts to introduce larger pores in sol-gel-derived silica biomaterials, though successful, resulted in mechanically weaker matrices that may not be useful for tissue engineering [16]. Therefore, sol-gel-derived silica biomaterials are primarily considered for drug delivery and bio-imaging applications [17–19].

Efforts to incorporate bioactive silica into the commonly used polymer matrices resulted in scaffolds with optimized pore, strength, and degradation features. Our work and that of others in the field continue to explore both natural and synthetic biodegradable polymers in an innovative way to create silica and other ceramic-incorporated three-dimensional porous structures for tissue engineering and regenerative medicine [15,20,21]. These silica composite scaffolds were designed to enhance bioactivity to promote mineralization and host tissue integration [22–24]. The recent additive manufacturing process has paved the way to develop various ceramic and amorphous silica biomaterials and structures for tissue engineering [25,26]. These efforts were successful in introducing pore properties into ceramics and Bioglass-based biomaterial systems by combining with polyesters such as poly(lactic acid) (PLA), poly(caprolactone) (PCL), and their copolymers known to produce acidic degradation byproducts leading to tissue necrosis and implant failure *in vivo* [27–30].

Therefore, the goal of this study is to develop a silica-based biomaterial that has the beneficial features of Bioglass for tissue engineering purposes and is yet porous, biodegradable, hydrophilic, and fibrous. It is known that the amorphous form of silica is bioactive and degradable compared to the crystalline counterpart, quartz [11]. We hypothesize that consolidation of amorphous silica fibers can lead to the synthesis of a matrix system that is a three-dimensional fibrous network mimicking the native ECM structurally while absorbing high water content like a hydrogel without altering its structural dimension and strength. Additionally, this silica fiber-processing methodology will enable us to combine other additives including bioactive glasses, ceramics, and polymers to manipulate final matrix properties to meet the needs of a particular tissue engineering application. In this manuscript, we report a methodology that is efficient to synthesize amorphous silica fiber matrices and study the effect of processing temperature and additives on matrix physicochemical properties and *in vitro* osteogenic ability.

2. Materials and methods

2.1. Amorphous silica fiber scaffold biomaterials

Approximately 50 g of pure amorphous silica fibers with fiber diameters of 10 μm (McAllister Mills, VA) were blended at 50,000 RPM for 30 min to fragment the fibers and form a slurry. The fiber slurry was washed in 5 mM HCl solution for 2 h to remove any contaminants, filtered, and washed twice in distilled water (dH_2O). Subsequently, the fibers were re-suspended in 1 L of dH_2O , placed into a 12 cm \times 12 cm mold, and pressed to remove approximately 50% of the excess water. The mold was then placed into an oven and dried at 110 $^\circ\text{C}$ overnight, to remove the remaining water. The resulting green body was then placed into a high-temperature oven and sintered at varying temperatures (1,350, 1,450, 1,550 $^\circ\text{C}$) with a ramp rate of 3 $^\circ\text{C}$ per minute with a dwell time of 2 h. Afterward, the sintered scaffolds were cooled quickly to room temperature to prevent crystallization of the silica fibers.

To fabricate silica fiber scaffolds with cellulose, 12.5 g (20 wt% cellulose) of cellulose fibers (CF) (Sigma-Aldrich, MO) were added to 50 g of silica and blended to fragment the fibers. The slurry was then treated with 5 mM HCl, washed, and dried as described above. Before sintering the silica fibers, to ensure complete thermal decomposition of the cellulose additive, the green body was heated at 800 $^\circ\text{C}$ for 1 h. Then the sample was heated to 1,550 $^\circ\text{C}$ and the silica fibers were sintered for

2 h. To study the role of PVA as an additive, 12.5 g of PVA (20 wt% PVA) (Sigma-Aldrich, MO) was dissolved in 1 L of dH_2O , then the fragmented and washed silica fibers were added to the PVA solution and homogenized. The resulting slurry was then pressed and dried at 110 $^\circ\text{C}$ overnight. This formed green body was heated to 800 $^\circ\text{C}$ and kept at this temperature for 1 h then sintered at 1,550 $^\circ\text{C}$ for 2 h to ensure complete thermal decomposition of PVA, just as was done for the silica fibers with 20 wt% cellulose samples.

2.2. Matrix morphology, water absorption, and porosity

Qualitative overview of the silica scaffold morphologies and the effects that sintering temperature and additives caused were obtained using scanning electron microscopy (SEM). The samples were sputter-coated with gold/palladium (E5100, Polaron) and examined using Nova NanoSEM 450 (FEI). Energy-dispersive X-ray spectroscopy (EDS) was also conducted on silica scaffold samples with cellulose/PVA additives before and after sintering to confirm the presence or absence of the sintering additives that were used. Oxford Aztec Energy Microanalysis System with X-Max 80 Silicon Drift Detector was used to determine atomic composition and distribution in the samples.

Silica fiber scaffolds of approximately 80 mg were also dried in a 120 $^\circ\text{C}$ oven for 2 h, then submerged in 20 mL of dH_2O and weighed. The resulting hydrated mass was then compared with the dried weight according to the following equation to calculate the matrix water absorption.

$$\text{Water Absorption (wt\%)} = \frac{\text{Wet Weight (mg)} - \text{Dry Weight (mg)}}{\text{Dry Weight (mg)}} \times 100 \quad (\text{Eq.1})$$

For quantitative analysis of the silica scaffolds' porosity and average pore sizes, the silica scaffolds were subjected to mercury porosimetry (AutoPore IV Mercury Porosimeter, Micromeritics). Cylindrical scaffolds with 10 mm diameter and 20 mm height were used for the analysis ($n = 6$). The samples were placed into the porosimeter where vacuum was applied and pressures ranging from 0.1 to 2 atm were applied for mercury intrusion. Mercury intrusion and the total amount of mercury used in relation to bulk sample size was then used to determine the average pore diameter and overall porosity [31,32].

2.3. Matrix mechanical characterization

To assess the mechanical properties of the silica fiber scaffolds and the effects that sintering temperature and additives cause, compression testing was conducted. The testing was performed according to ASTM D695-15 standards, where cylindrical samples with 10 mm diameter and 20 mm height were used for analysis ($n = 6$) [33]. The samples were loaded onto a Tinius Olsen I50KS (Tinius Olsen Inc., PA) and compressed until 50% compression at a rate of 2 mm/min. The compressive modulus was calculated by plotting the stress-strain curve, and the slope of the linear region was calculated and taken as the compressive modulus. Also, the 0.2% offset yield strength was calculated, as the transition between the linear region of the stress-strain curve and the plastic deformation region of the stress-strain curve was not immediately clear [33]. To obtain the 0.2% offset yield strength, a straight line (initiated at the strain of 0.2%) was drawn parallel to the initial linear region of the graph and extended until it intersected the stress-strain curve, and the stress value at the intersect was determined to be 0.2% offset yield strength.

2.4. Matrix degradation

To verify that the developed silica scaffolds are degradable, an *in vitro* degradation experiment was conducted. Silica scaffold samples weighing approximately 80 mg were placed in 50 mL of phosphate-

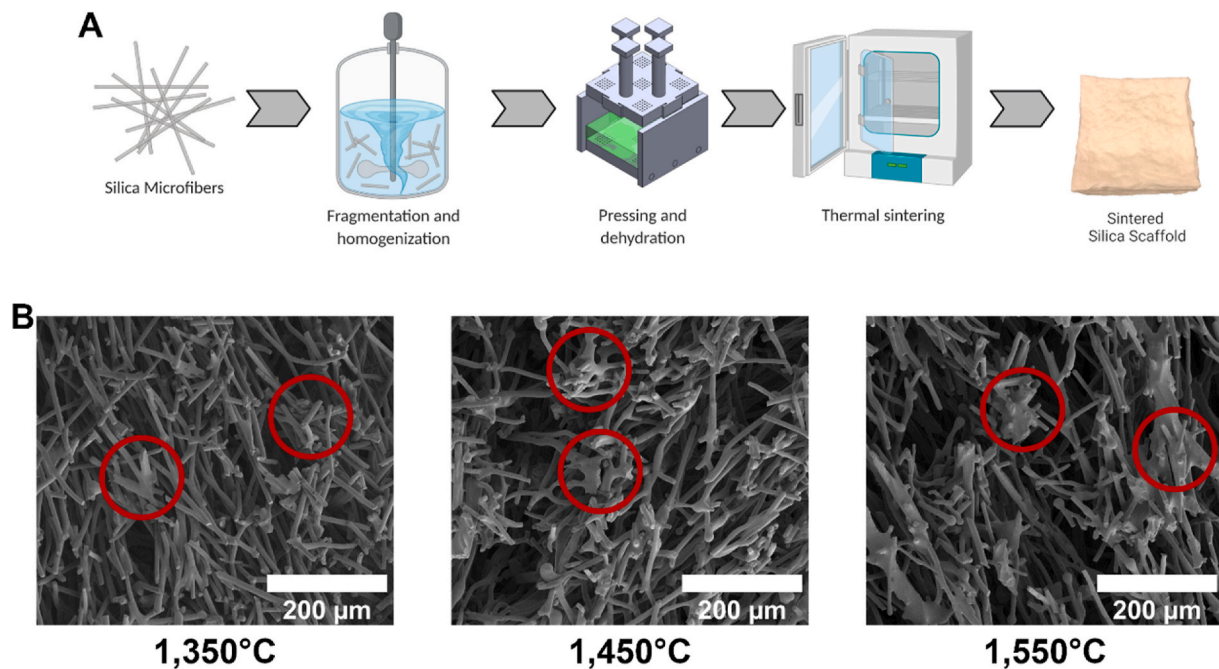


Fig. 1. The effect of sintering temperature on silica fiber scaffold fabrication. A) Schematic of silica fiber sintering process. The fibers are blended and homogenized, then pressed and dried in a mold, and sintered at varying temperatures (1,350, 1,450, and 1,550 °C). B) SEM images of resulting silica fiber scaffolds. The scaffolds sintered at higher temperatures showed more complete sintering of adjacent silica fibers, while the scaffolds sintered at lower temperatures showed incomplete sintering of adjoining silica fibers. The sintering joints are highlighted by the red circles. The scaffolds sintered at higher temperatures also show larger pore spaces when compared to the scaffolds sintered at lower temperatures.

buffered saline (PBS) and maintained at 47 °C. The elevated temperature was used to accelerate the degradation process to make the experiment more feasible in a laboratory setting and an increase of 10 °C can be approximated to accelerate degradation by a factor of 2 [34]. The samples were removed, washed, dried, and weighed weekly, and the degradation media were replaced weekly to maintain sink conditions.

2.5. *In vitro* cytocompatibility assessment

The osteocompatibility of the silica fiber matrices was assessed *in vitro* via culture with human bone marrow-derived mesenchymal stem cells (hMSCs). The hMSCs were isolated from freshly isolated human bone marrow aspirate with proper ethical controls and consent obtained by the supplier (hBMA; Lonza, Switzerland) as described previously [20, 21]. Briefly, hBMA was concentrated using the Magellan® system (Arteriocyte, MA), plated in 150 mm tissue culture plates (TCP), and placed in a 37 °C humid environment with 5% CO₂. The adherent cells were then isolated and cultured in growth media consisting of Dulbecco's Modified Eagle Medium with Ham's F12 with Glutamax (DMEM/F12+GlutaMAX; Life Technologies, CA) supplemented with 10% fetal bovine serum and 1% penicillin-streptomycin (Life Technologies, CA). The medium was changed every two days and hMSCs were passaged at 80–90% confluence. The pluripotency of the isolated hMSCs has been confirmed previously via the trilineage differentiation assessment [20]. Passage 3 cells were used for this study.

Silica scaffolds sintered at 1,550 °C without any additives were cut into disks with 10 mm diameter and 3 mm height, autoclaved, and seeded with 25,000 hMSCs. The seeded scaffolds were then cultured in osteogenic media consisting of DMEM/F12+GlutaMAX, 10% fetal bovine serum, 1% penicillin/streptomycin, 10 nM dexamethasone, 10 μg/mL ascorbic acid, and 10 mM β-glycerophosphate [20]. The seeded scaffolds were cultured in an incubator (Heracell™ VIOS 160i; Thermo Fisher, MA) at 37 °C with 5% CO₂, with the media changed every 2–3 days. hMSCs cultured in 24-well TCP were used as the control groups.

For qualitative analysis of cell proliferation and cell attachment,

hMSC-seeded silica scaffolds were subjected to Live/Dead staining and SEM imaging after 1, 7, and 14 days of culture. Live/Dead staining was conducted using LIVE/DEAD™ Viability/Cytotoxicity Kit (Thermo Fisher, MA) according to the manufacturer's protocol. The stained samples were imaged using a fluorescent microscope with 494/517 nm excitation/emission for calcein-AM (Live) and 528/617 nm excitation/emission for ethidium homodimer-1 (Dead). For SEM imaging, the samples were fixed using 1% glutaraldehyde for 1 h at room temperature, then 3% glutaraldehyde overnight at 4 °C. The samples were then washed and dehydrated by equilibrating with 50, 70, 90, and 100% ethanol in sequential order and dried. Thus prepared samples were sputter-coated (E5100, Polaron) and then imaged using NanoSEM 450 (FEI).

To quantify the proliferation of seeded hMSCs, the dsDNA concentration of each sample was measured using Quant-iT™ PicoGreen™ dsDNA Assay Kit (Thermo Fisher, MA). Silica samples seeded with cells and the hMSCs cultured on 24-well plates were removed from culture after 1, 7, 14, and 21 days (n = 3), and lysed using 1% Triton X-100 and repeated freeze-thaw cycles. Afterward, the lysates were prepared using a previously reported protocol [21,35,36], and sample fluorescence was measured at 485/535 nm excitation/emission using a Synergy HT plate reader (BioTek Instruments, VT).

2.6. ALP activity and Alizarin red staining

Basic osteogenic assays were conducted to verify bone tissue engineering as a possible use for the developed silica matrix. Alkaline Phosphatase (ALP) activity and Alizarin Red Staining/Quantification were used to quantify the degree of osteogenic differentiation on the seeded hMSCs. ALP activity was measured using cell lysates from samples after 1, 7, 14, and 21 days of culture (n = 3) and the ALP substrate kit (Bio-Rad, CA) as previously reported [35]. Briefly, the cell lysates were combined with p-nitrophenyl phosphate (p-NPP) and incubated for 30 min at 37 °C. The reaction was stopped by adding 0.4 M NaOH, and the absorbance of the resulting solution was read at 405 nm using a

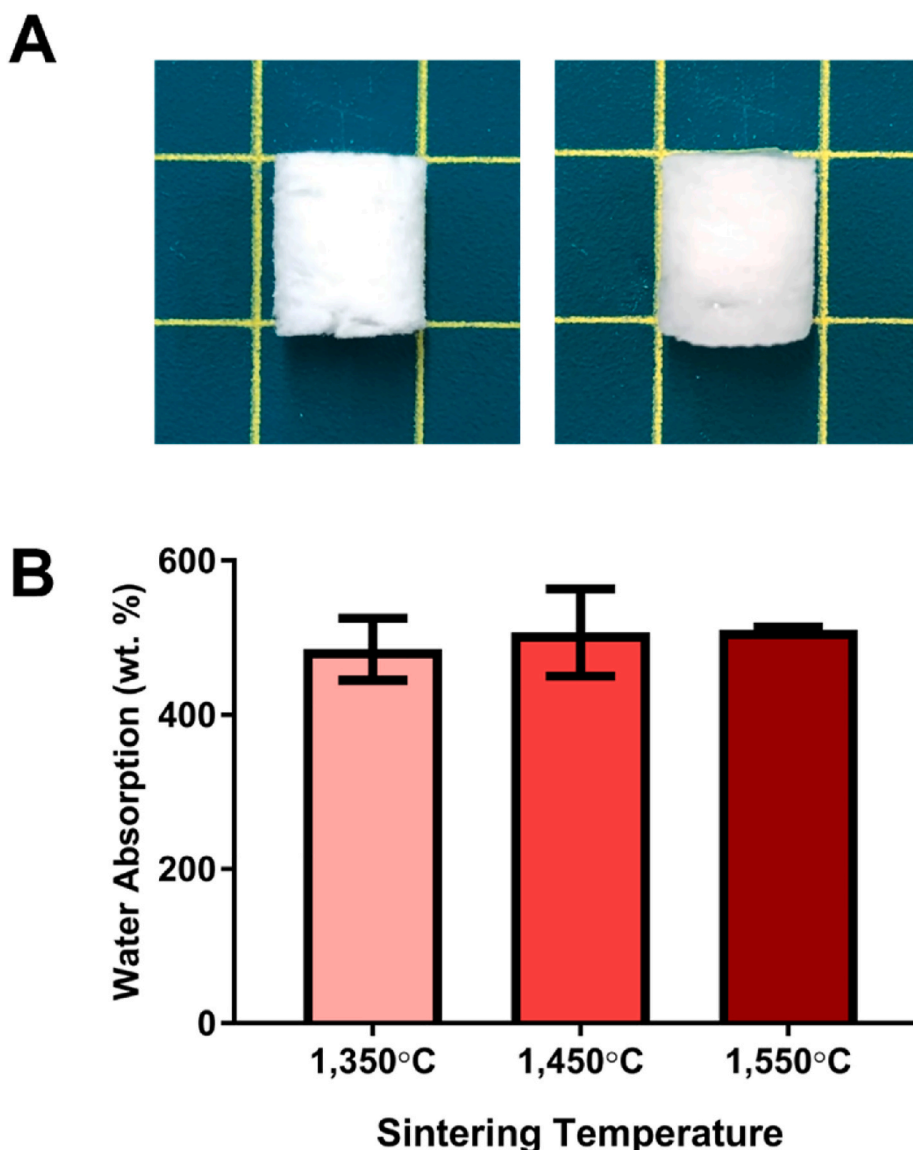


Fig. 2. Amorphous silica fiber scaffold water absorption. A) Images of silica scaffolds sintered at 1,550 °C before and after water absorption shows that no changes to the overall structure or volume occurred. B) Water absorption quantification for the fiber scaffolds sintered at varying temperatures shows that silica scaffolds are capable of absorbing approximately 500% of their weight when soaked in water regardless of sintering temperature ($n = 3$).

microplate reader (Synergy HT; BioTek Instruments, VT). The results were then normalized with the corresponding dsDNA concentration obtained from the PicoGreen assay. Cell-induced mineralization was assessed through Alizarin Red staining and quantification of the seeded scaffolds after 7, 14, and 21 days in culture ($n = 3$). The samples were washed with PBS, fixed with 70% ethanol for 20 min at 4 °C, stained with 40 mM Alizarin Red dye (Sigma-Aldrich, MO) at pH 4.23 for 10 min, and washed with dH₂O. Acellular samples were also subjected to Alizarin Red staining to account for non-cell-induced mineralization of the scaffolds. To quantify the degree of Alizarin Red staining, 10% cetylpyridinium chloride (CPC; Sigma-Aldrich, MO) was added to solubilize the dye for 15 min at room temperature [35]. The absorbance of the resulting solution was then measured at 562 nm using a plate reader (Synergy HT; BioTek Instruments, VT). The readings from the corresponding acellular groups were then used to normalize the data.

2.7. Statistical analysis

Quantitative data presented in this work were analyzed using one-way or two-way analysis of variance (ANOVA), where appropriate,

followed by Tukey's Multiple Comparison Test. The data are represented as the mean \pm standard deviation, with p-values less than 0.05 used as the standard for being statistically significant.

3. Results and discussion

Three different sintering temperatures of 1,350, 1,450, and 1,550 °C were employed to determine the effect of temperature on the morphology, porosity, and mechanical properties of silica fiber scaffolds. Also, the effects of sintering additives were assessed with the inclusion of cellulose fibers and PVA along with the silica fibers into the green body. PVA was used as a binder material that would provide strength to the silica fibers during the pressing and green body formation stages, as it has been used previously as a binder to sinter ceramic particles [37–39]. It was also noted that since the PVA is dissolved into the liquid phase of the slurry, some of the added PVA is lost during the pressing of the slurry, ultimately resulting in less than the originally added 20 wt%. Cellulose fibers were included in the silica green body to serve as a porogen for the silica fibers, where the spaces occupied by the cellulose fibers during the green body phase would be voided as the

Table 1
Comparison of developed silica fiber scaffold and traditionally used tissue engineering biomaterials.

Amorphous Silica Fiber Matrices	Hydrogels	Ceramic or Polymeric Matrices
Mechanically strong to support load-bearing tissue regeneration	Often soft and viscoelastic, not ideal for load-bearing tissue engineering [46,47]	Mechanically strong to support load-bearing tissue regeneration [56, 57]
Hydrophilic and porous nature allows up to 500 wt % water uptake	The level of hydration depends on the nature of the polymer, crosslinker, degree of crosslinking, and other factors [47]	Typically do not absorb water
Water absorption does not affect matrix/implant dimension	Swells in volume with hydration.	Limited hydration and swelling
>90% highly porous matrices with variable pore sizes ranging 50–200 μm	>99% highly porous with pores ranging 10 nm to 600 μm [58]	Fabrication and processing techniques allow variable pore size and overall matrix porosity [14,21]
Micrometer-sized pores can support cell infiltration, tissue ingrowth, and nutrient exchange needed for tissue regeneration	Macroporous hydrogels with large pore sizes can support cell infiltration [58–60]	Defined pore sizes can be created to support cell/tissue ingrowth and nutrient exchange for tissue regeneration [14, 15]
Matrix fibrous nature, high water content with micron-sized pores can closely mimic native extracellular matrix	Can mimic native ECM	Macro features fail to mimic native ECM
Biodegradable and provide long-term support (more than 2 years) for tissue regeneration	Degradation rate is dependent on the nature of the polymer, crosslinker, and crosslink density [61]	Variable degradation rate for certain polyesters and calcium phosphates, but polyesters tend to exhibit bulk degradation [62,63]
Easy to handle, store, and sterilize via heat and other approved sterilization techniques	Difficult to handle, store, and sterilize; Limited by Ozone and Ethylene Oxide sterilization methods that are only limited to surface or require complete processing in a sterile environment [64]	Feasible to apply all approved sterilization techniques with few exceptions with composites involving polymers such as PLA and PLGA via heat sterilization

cellulose decomposes during the sintering process. The voided pores, if large enough, would increase the average pore diameter and porosity, allowing for higher nutrient transport and cell infiltration into the silica scaffold. The two additives were also chosen as both materials have been noted to decompose into small volatile compounds at high temperatures, which minimizes the potential of impurities in the final scaffold [40–43].

The morphological changes due to sintering were analyzed via SEM (Fig. 1B). We observed that with increasing sintering temperature, the degree of sintering of the adjoining silica fibers is increased. As highlighted in the red circles, the scaffolds sintered at 1,350 $^{\circ}\text{C}$ show some degree of sintering between the adjacent silica fibers, but there were still silica fibers that had not been sintered completely with the neighboring fibers. The number of lone fibers decreased for the scaffolds sintered at 1,450 $^{\circ}\text{C}$, with most of the neighboring silica fibers sintering together to form sintered joints. The trend continued when the scaffolds were sintered at 1,550 $^{\circ}\text{C}$, where most, if not all, adjacent silica fibers were sintered together and formed into larger sintering joints. Also, in general, the increase in sintering temperature and degree of sintering seems to have resulted in the creation of larger pore sizes. The difference in pore structure is clear between the scaffolds sintered at 1,350 and 1,550 $^{\circ}\text{C}$, where the scaffold sintered at higher temperatures presented larger pores, which may have developed due to increased agglomeration of the silica fibers into the sintering joints (highlighted in the red

circles).

We also examined the water absorption of the developed silica fiber scaffolds (Fig. 2). Silica fiber scaffolds showed the ability to absorb water approximately 500% or 5 times their mass. These results are in stark contrast to polymer scaffolds that are often used for tissue engineering purposes, such as PLA and PLGA, which are hydrophobic by nature [44]. In addition, the scaffolds did not swell or change morphologically in contact with water which is the case for many hydrogels used for tissue engineering purposes [45,46]. The swelling properties of hydrogels result in rapid loss of mechanical stability of the material/implant due to dilution, and this may result in rapid and premature implant degradation at the site of regeneration [47,48]. In contrast, the developed silica scaffolds are capable of absorbing a significant amount of water, while maintaining their overall shape and pore structure, which provides the aqueous environment needed for cell growth/infiltration and nutrient transport. Silica biomaterials have been known to be hydrophilic due to the presence of silanol (Si-OH) groups on the surface of the material [48], and the capillary pore structure of the developed matrix may be the cause for the high water absorption seen for the silica fiber scaffolds. Additionally, silica fiber matrices can be easily sterilized (via autoclaving), stored, and processed for the desired application, while hydrogels and biodegradable polymer-based matrices need to go through complex sterilization and storage protocols [64]. The unique aspects of the amorphous silica fiber scaffolds in comparison with some of the traditional scaffold options (hydrogels, polymer/ceramic systems) are listed in Table 1.

The morphologies of the silica scaffolds with additives before and after sintering were also assessed through SEM (Fig. 3B). The SEM images of the silica fibers before sintering clearly show the presence of sintering additives, with the cellulose fiber additive seen wrapping around the silica fibers and the PVA shown forming films connecting the silica fibers. Also, it was noticed that the PVA additive group produced firm and more solid green bodies than the other groups, presumably due to the presence of PVA in the solid phase that held the silica fiber scaffolds together. In the case of cellulose fiber addition, the silica scaffolds with cellulose showed a similar degree of sintering when compared to that of the pure silica scaffold sintered at 1,550 $^{\circ}\text{C}$, where the majority of the adjoining silica fibers were sintered together to form sintering joints. On the other hand, the silica fibers with PVA showed higher levels of sintering with larger sintering joints. This may be due to the shrinkage and compaction of the silica fibers that occurred during the drying process. PVA is a water-soluble polymer and it coats silica fibers and helps in compacting fibers whereas cellulose fibers not soluble in water are dispersed in the slurry. As the PVA in the liquid phase dried, it formed thin films that connected the neighboring silica fibers, as evidenced in the SEM images of the green body pre-sintering, resulting in overall compaction of the green body and higher levels of sintering and agglomeration of those compacted silica fibers.

The mechanical properties, compressive modulus and yield strength, of the silica fibers under compression were also measured (Fig. 3C and D). The compressive moduli of the pure silica fiber scaffolds increased from 9 to 13 MPa with increasing sintering temperature. This trend may be due to the formation of more complete sintering joints when the silica fibers were sintered at higher temperatures. Meanwhile, the yield strength of the silica matrices sintered at different temperatures varied between 0.5 and 1 MPa and did not show any significant differences or noticeable trends. Also, the addition of cellulose did not significantly increase either the compressive modulus or the yield strength of the final silica scaffolds, remaining similar to the compressive modulus and yield strength of the pure silica matrix sintered at 1,550 $^{\circ}\text{C}$. However, the inclusion of PVA during the sintering process resulted in statistically significant increases to both the compressive modulus and yield strength of the scaffolds, with increases of approximately 94% and 45% to its compressive modulus and yield strength, respectively, when compared with that of the pure silica matrix also sintered at 1,550 $^{\circ}\text{C}$. This increase in mechanical properties when PVA is introduced during the fabrication

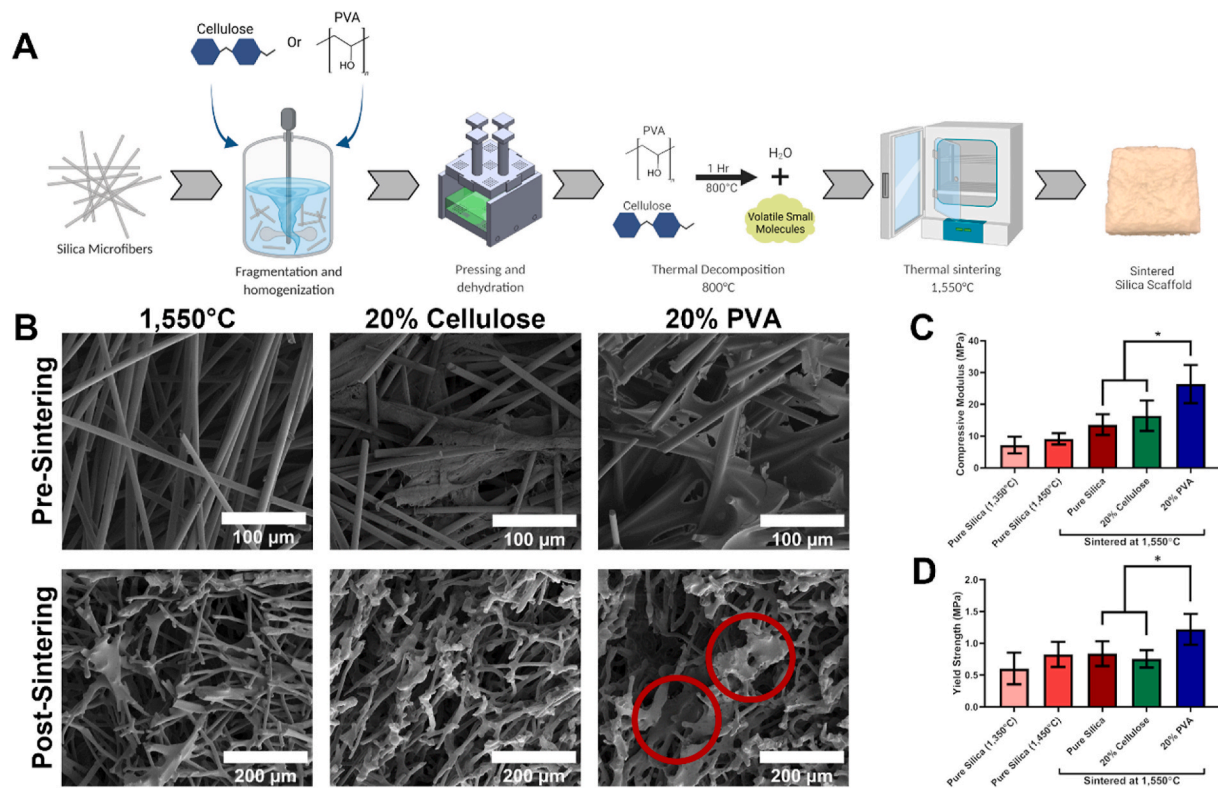


Fig. 3. Effect of sintering additives during silica scaffold fabrication. A) Cellulose fiber or polyvinyl alcohol (PVA) was added to the silica slurry during the homogenization process, then pressed, dried, and fired at 800 °C before sintering at 1,550 °C. B) SEM images of the silica scaffolds before and after sintering. The pre-sintering images show the presence of cellulose interspersed between the silica fibers. The addition of PVA and subsequent drying of the slurry resulted in formation of films of PVA in between the silica fibers as the slurry was dried. The post-sintering images show that scaffolds with 20% PVA resulted in more complete sintering of the silica fibers and much smaller pore sizes (highlighted within red circles). C and D) Mechanical testing of the silica fibers sintered at varying temperatures and with addition of additives ($n = 6$). The addition of PVA resulted in significantly higher compressive modulus and yield strength than all other groups, while the addition of cellulose fibers did not significantly affect the compressive modulus of silica scaffolds (C). Variations in sintering temperature did not significantly change the compressive moduli of scaffolds. Meanwhile, changes in sintering temperature and addition of cellulose did not result in significant change to the scaffold's yield strength (D). Asterisks denote significance of $P < 0.05$.

process may be attributed to the increased sintering of neighboring fibers resulting in densification of the silica scaffold, evidenced by decreased pore characteristics, and formation of larger sintering joints, as evidenced in the SEM images of the scaffolds after sintering (Fig. 3B), and these joints may have facilitated the resistance to deformation during compression. These results also indicate that by increasing the degree of sintering and densification, the mechanical properties of the silica scaffold can also be increased, either through the addition of PVA to facilitate compaction or by creating denser green bodies by pressing more water out of the slurry before dehydration. Also, although the results were not statistically significant, it may be possible to increase either the sintering temperature or the sintering duration to increase the amount of sintering, thereby increasing the mechanical properties of the silica scaffolds.

Elemental analysis of the silica fibers with additives before and after sintering via EDS was also conducted to verify the complete decomposition of additives after sintering (Fig. 4). The elemental compositions and mapping of the samples before sintering did note the presence of organic material, carbon atoms, along with the silica fibers, presumably cellulose and PVA. However, after sintering, minimal levels of carbon were detected, attributed to the background presence of carbon within the environment surrounding the samples. The only other signals that were detected were those corresponding to the silicon and oxygen of the silica fibers, as well as gold used to sputter coat the samples before imaging. Therefore, the complete thermal decomposition of the additives was achieved during the sintering process, which ultimately resulted in a pure amorphous silica fiber scaffold after the final sintering

step.

To quantitatively assess the morphology and pore structure of the silica scaffolds, we conducted mercury intrusion porosimetry (MIP) (Fig. 5). The average pore diameter of the silica scaffolds increased with increasing sintering temperature (Fig. 5A). The silica scaffolds sintered at the lowest temperature, 1,350 °C, resulted in average pore diameters of 67.78 μm that increased up to 89.80 μm for the scaffolds sintered at 1,550 °C. The change in overall pore size distribution is also clear in the pore size distributions (Fig. 5C), where the relative distributions of pore sizes increase with an increase in sintering temperature. The quantitative analysis of the pore sizes confirms the observations noted in the qualitative SEM images of the matrix morphology. This increase in average pore size may be due to the higher degree of agglomeration and fusion of nearby silica fibers sintered at higher temperatures. The increased fusion would result in larger void areas, subsequently increasing the size of pores (in the size range of 100–200 μm) throughout the scaffold. As reported in the literature, pore sizes in the 50–300 μm range are essential for cell infiltration and adequate nutrient transport that can support the complete cellularization of the implant [13–15]. Therefore, the presence of pores in this optimal size range in the sintered silica matrices demonstrate the potential value of the developed silica matrix as a new class of fibrous silica biomaterial for tissue engineering purposes.

Also, MIP analysis showed that the addition of cellulose did not significantly alter the average pore diameter of the silica scaffolds when compared with that of the pure silica group (Fig. 5A). This result shows that the added cellulose did not act as a porogen that would create larger

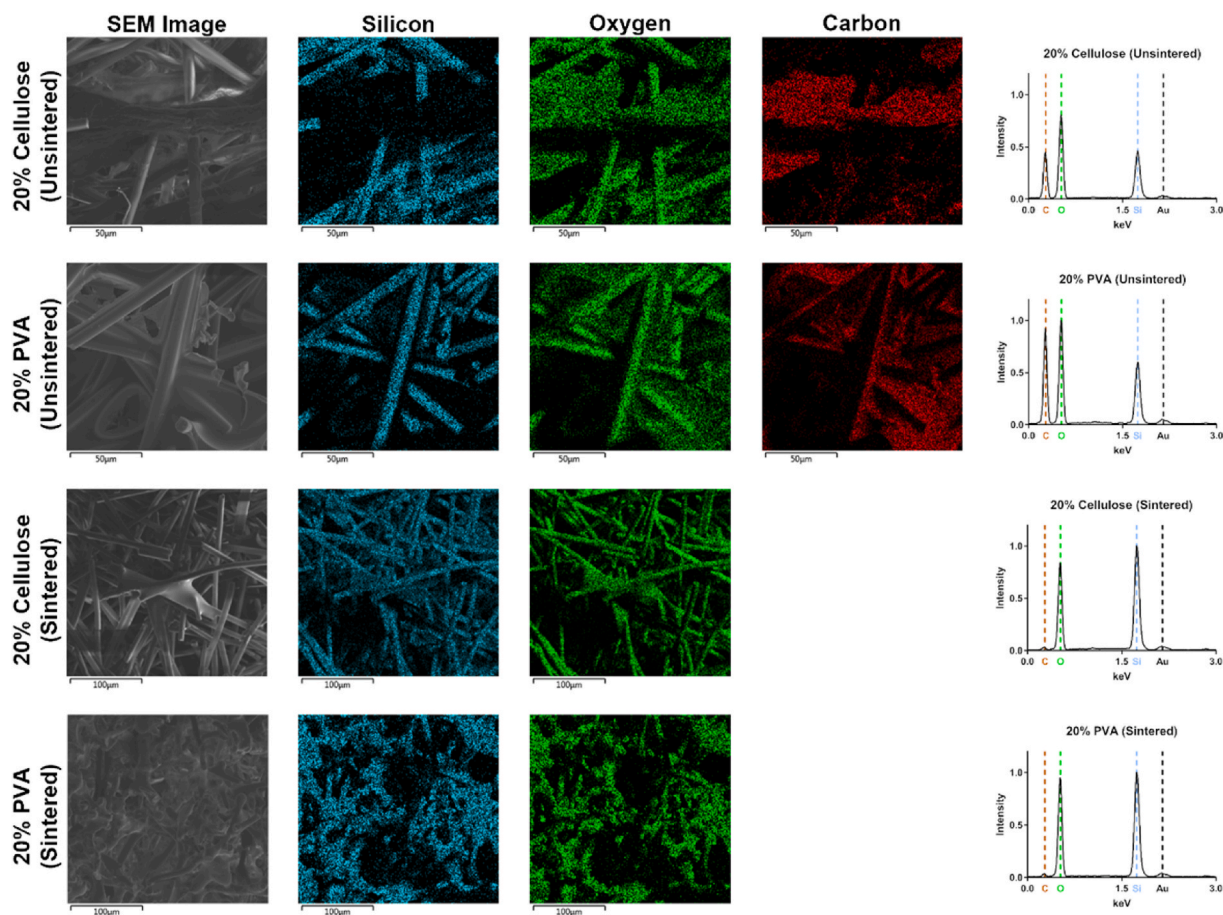


Fig. 4. Energy dispersive X-ray (EDS) analysis of silica scaffolds with additives before and after sintering. The distribution of atoms present in the samples show that after sintering, both the cellulose fiber and PVA additives have been removed via thermal decomposition after sintering. The spectra recorded show the presence of silicon and oxygen as part of the silica fibers, and carbon atoms present as part of the additive, which are reduced to trace levels post-sintering. The presence of gold atoms is due to the coating of the samples prior to SEM and EDS analysis.

voids as it decomposed. This may be due to the overall size and structure of the added cellulose. As shown in the SEM images of the silica fibers with cellulose before sintering (Fig. 3B), the cellulose particles were seen to be wrapped around the silica fibers and did not occupy a significant portion of the green body matrix. This indicates that the added cellulose did not take up any additional space, but rather settled into voids that were already present in the silica fiber matrix, resulting in minimal changes to the overall morphology and pore structure of the scaffolds. This suggests the need for the use of larger cellulose particles to serve as porogen. On the other hand, the addition of PVA resulted in a significant reduction in the average pore diameter of the scaffold, resulting in a 31% reduction in the average pore diameter (Fig. 5A). The resulting average pore diameter was the lowest out of all groups that were studied and may be due to the compaction during the drying stage and significant sintering/densification of the silica fibers. As mentioned previously, the inclusion of PVA resulted in the compaction of the green body due to the solidification of the PVA around the silica fibers, which may have resulted in an overall decrease in the void space between the silica fibers.

The overall porosity of the silica fiber scaffolds for all groups fell into the range of 85–94% porosity (Fig. 5B). The similarities in porosity, despite the differences in the average pore diameter for the pure silica scaffolds that were sintered at varying temperatures, may be because the silica scaffolds with smaller average pore diameters had more of the smaller sized pores, while the scaffolds with higher average pore diameters had fewer pores but the average size of the pores was greater, resulting in similar overall porosities. These results also correspond with

the fact that the same amounts of silica fibers were used to create these silica fiber scaffolds, which were of the same dimensions. As for the silica scaffolds with cellulose as an additive/porogen, the overall porosity was not statistically different when compared to the pure silica scaffold, which further reinforces that the cellulose additive did not contribute to the formation of more pores and rather settled into the void spaces already present in the silica fiber matrix. However, as for the silica scaffolds with PVA used as an additive, the overall porosity of the resulting scaffolds was significantly lower than that of the pure silica fiber (85% vs. 93%). This may be due to the compaction of the green body as mentioned before, which lowered scaffold average pore diameter, increasing the degree of sintering, and increasing the overall mechanical properties of the silica scaffolds. Overall, the porosimetry data indicate that a highly porous scaffold (about 90%) could be produced, which would facilitate cellular infiltration and nutrient transport that is necessary for the complete cellularization of the scaffold. In addition, the high degree of porosity presents a larger surface area for silica fiber degradation to occur, circumventing one of the weaknesses of Bioglass and other melt-derived silica biomaterials.

By analyzing the morphology, porosity, and mechanical characteristics, pure silica fiber scaffolds sintered at 1,550 °C were used as the scaffold group for the remainder of the study. This scaffold group showed the most complete sintering between adjacent silica fibers and presented the highest average pore size. Although it was not statistically significant, its mechanical properties were higher than the other pure silica fiber scaffolds sintered at lower temperatures. Also, the silica scaffolds with PVA additives were not used despite their high

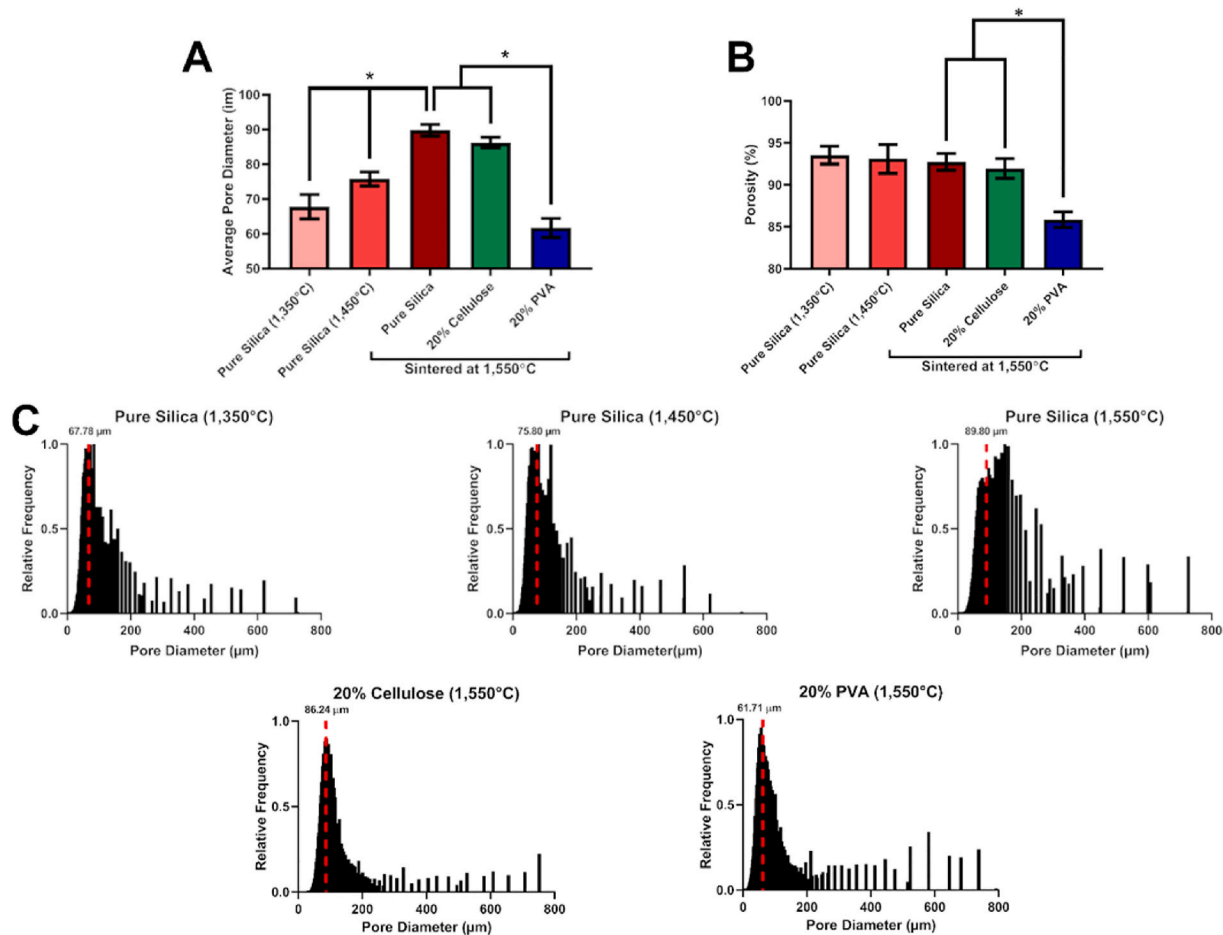


Fig. 5. Mercury intrusion porosimetry of silica scaffolds. A) Average pore diameter of silica scaffolds ($n = 6$). The average pore diameter increased significantly with increases in sintering temperature, with the scaffolds sintered at 1,550 °C showing the highest average pore diameter. Addition of cellulose fibers to the scaffolds did not significantly alter the average pore diameter when compared with the scaffolds sintered at 1,550 °C. However, the addition of PVA to the scaffold fabrication process resulted in significant decreases in the average pore diameter of the scaffolds. B) Average porosity of silica scaffolds ($n = 6$). The overall porosity of the silica scaffolds did not change with sintering temperature showing porosities of approximately 90%. Addition of cellulose did not affect the porosity of the scaffold, while the addition of PVA resulted in significant decrease to overall porosity of the scaffold. C) Relative distribution of pore diameter of the silica scaffolds ($n = 6$). The dotted red line indicates the average pore diameter of each group. Asterisks denote significance of $P < 0.05$.

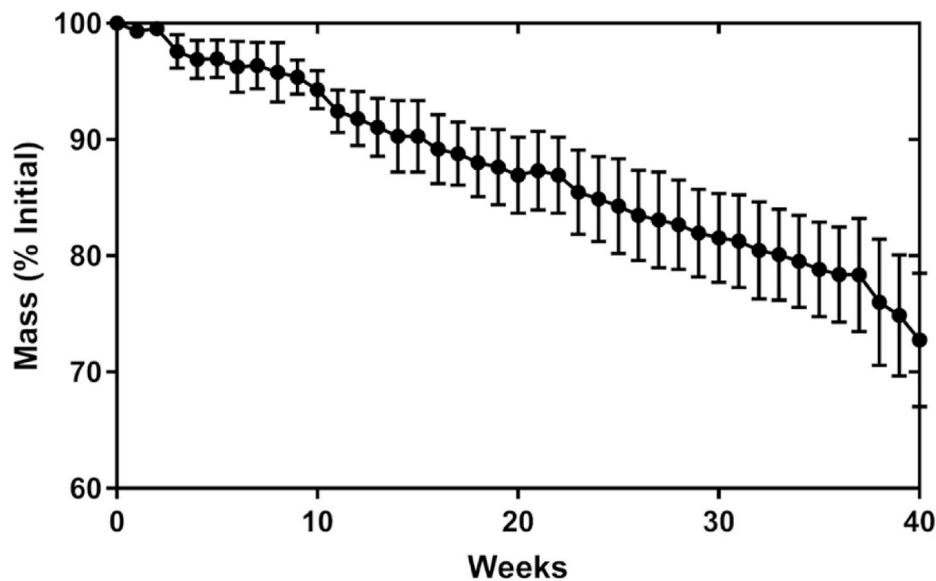


Fig. 6. Degradation profile of silica fiber scaffolds. Silica scaffolds were placed in PBS at 47 °C, and maintained in sink conditions via degradation media change every week. The degradation profile shows a gradual decrease in overall mass, reaching approximately 70% of its original volume by week 40 ($n = 3$).

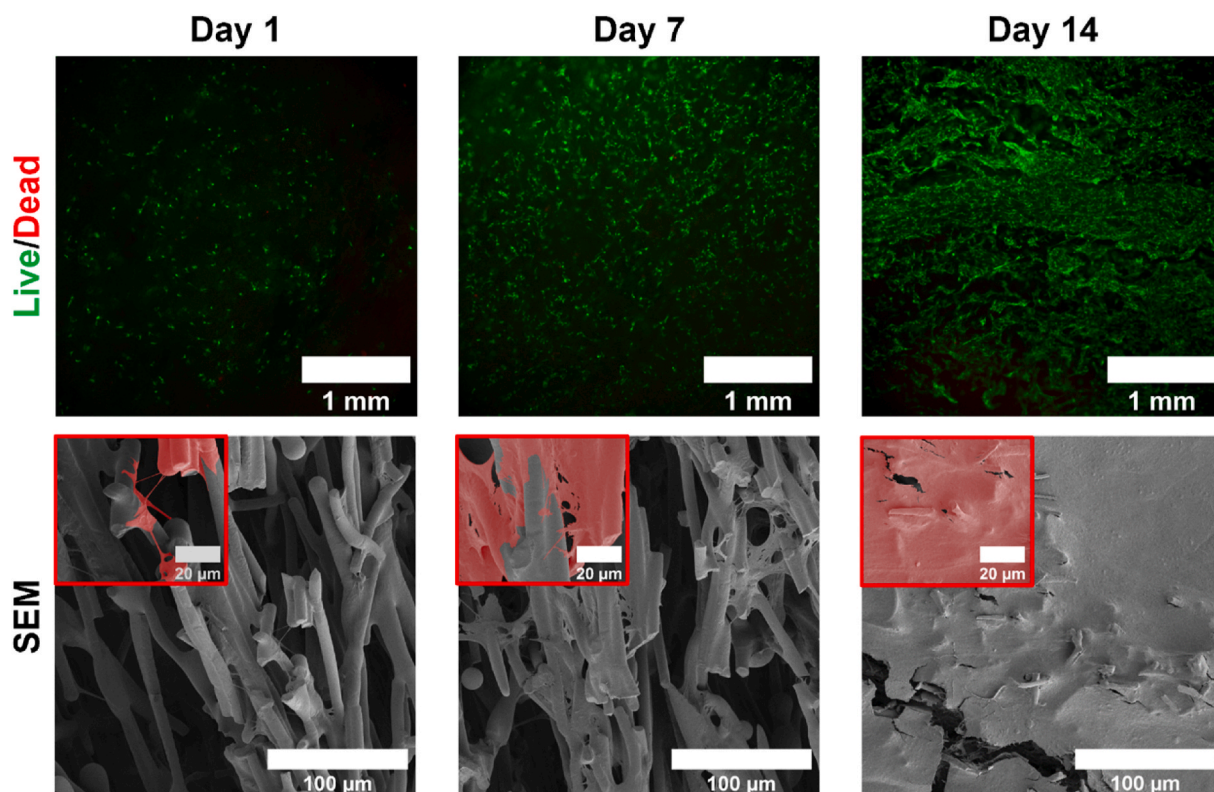


Fig. 7. In vitro assessment of silica fiber scaffold biocompatibility. A) Live/Dead and SEM images of silica scaffolds 1, 7, and 14 days after seeding with hMSCs. Live/Dead imaging shows minimal cell death and rapid proliferation of the seeded cells. SEM imaging also shows the same trend, with the cells reaching confluence by day 14. The inserts show close-ups of the cell attachment to the silica fibers, with the cells highlighted in red.

mechanical properties as the smaller pore sizes may negatively impact cell infiltration and nutrient transport [13].

The degradability of the developed silica scaffolds in an aqueous environment was also examined to further verify its usefulness as a new biomaterial for tissue engineering. As mentioned previously, the lack of *in vivo* degradation of Bioglass and other melt-derived glasses has prevented their use as a tissue engineering vehicle, despite their high biocompatibility and osteoinductivity [10,11]. On the other hand, the silica fiber scaffolds developed in this study were shown to degrade gradually in a linear manner when exposed to an aqueous environment (Fig. 6). The scaffolds were able to degrade and lose approximately 30% of their mass over 40 weeks, without any evidence of sudden changes in their mass. Macroscopic observations also did not show any evidence of structural failure or sudden deterioration of the silica scaffolds. These results indicate that the silica fibers degrade via a gradual surface erosion mechanism. This observation is in contrast with many other biodegradable polyesters that are commonly used to develop engineered structures for tissue repair/regeneration. For example, PLGA often undergoes bulk degradation wherein the material rapidly loses mass and structural integrity after a certain period in an aqueous environment, caused by autocatalysis of the material due to accumulation of its acidic degradation byproducts [27,28]. Meanwhile, the degradation mechanisms of amorphous silica biomaterials have been established, where amorphous silica is degraded gradually due to dissolution into silicic acid ($\text{Si}(\text{OH})_4$) in an aqueous environment [49,50]. However, the dissolution rate is exceedingly slow and requires ample surface area in contact with water to result in significant levels of dissolution. Also, the degradation byproducts of silica in an aqueous environment, (predominantly $\text{Si}(\text{OH})_4$) are reported to be biocompatible and are shown to induce the production of factors that encourage the proliferation and differentiation of surrounding cells [49,50]. It is important to note that this experiment was conducted at an elevated temperature, 47 °C, which indicates that the actual degradation rate of the material may be lower

than what is shown in Fig. 6 [34]. Although it is ideal for a tissue engineering scaffold's degradation rate to match the rate of new tissue formation, a slower rate of scaffold degradation may be advantageous in many cases as it provides structural support throughout the regeneration process, which is critical for certain types of tissue engineering fields, such as bone and osteochondral tissue engineering.

After confirming the degradability of the silica fiber scaffolds, a preliminary analysis of the developed scaffold's biocompatibility was conducted *in vitro* using qualitative imaging of cell viability and attachment through Live/Dead staining and SEM imaging (Fig. 7). The Live/Dead images show minimal cell death, evidenced by the prevalence of live green signal and the lack of red signal. It was also seen that the cells proliferated rapidly between 1 and 14 days of culture, reaching what seems to be confluence at 14 days. This is also confirmed through SEM imaging where the cells are attached to silica scaffold sparsely 1 day after seeding and proliferate rapidly until day 14 where the cells reach confluence, evidenced by the sheet of cells that cover the surface of the silica scaffold. This trend was quantitatively demonstrated through PicoGreen dsDNA quantification (Fig. 8A). The hMSCs seeded on silica fiber scaffolds showed high levels of proliferation at days 7 and 14, shown through an increase in dsDNA concentration. The dsDNA concentration then plateaued between days 14 and 21, presumably due to the cells reaching confluence and/or entering the differentiation cycle. It was also noted that cell proliferation was similar between the hMSCs cultured on silica scaffolds versus those cultured on TCP at 1, 7, and 14 days of culture, but significantly higher after 21 days of culture.

The comparable levels of cell proliferation between the hMSCs cultured on the silica matrix versus the cells cultured on TCP and the lack of cytotoxicity shows the high levels of cytocompatibility of the silica matrix that demonstrate its value as a new biomaterial for tissue engineering purposes. In addition, the morphological and mechanical properties of the matrix and its variability also show its potential as a new type of biomaterial that may be used for a variety of applications.

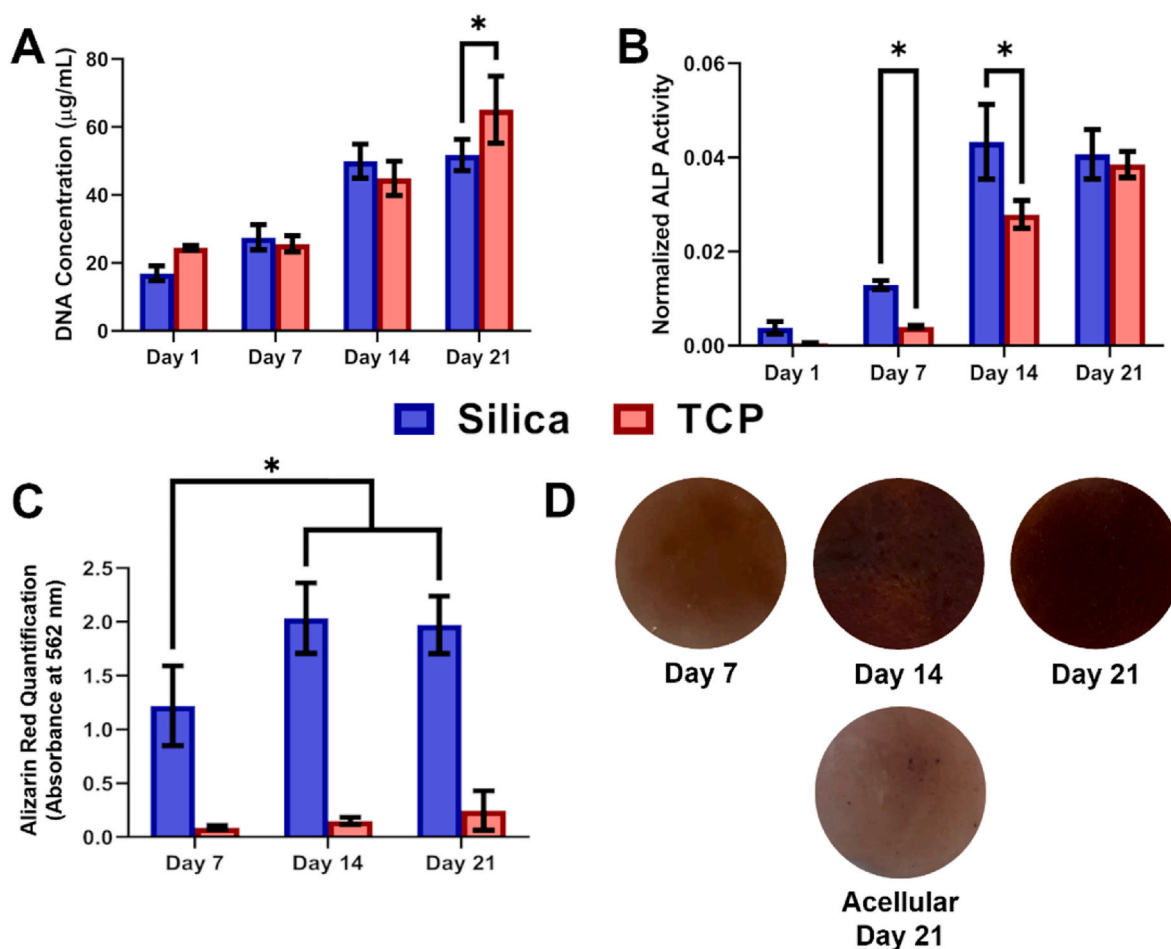


Fig. 8. *In vitro* osteogenic properties of silica fiber scaffolds. A) PicoGreen dsDNA quantification of hMSCs cultured on silica scaffolds or TCP after 1, 7, 14, and 21 days. The increases in DNA content correspond to the cell growth seen in Live/Dead and SEM images, where hMSCs seeded on silica reach confluence after 14 days, followed by a period of minimal proliferation between Days 14 and 21. B) Alkaline phosphatase (ALP) activity assay of hMSCs seeded on silica scaffolds or TCP normalized with DNA content ($n = 3$). The cells seeded on silica scaffolds showed significantly higher levels of ALP activity than cells cultured in TCP on Days 7 and 14. The earlier increase in ALP activity of cells seeded on silica scaffolds may indicate osteogenic properties of the developed silica scaffolds. C) Alizarin Red staining and quantification ($n = 3$). Alizarin red staining of hMSC-seeded silica scaffolds and TCP showed significantly higher levels of cell-induced mineralization at all timepoints (Days 7, 14, and 21). The results were normalized with an acellular silica scaffold and TCP control group. D) Photographs of silica scaffolds seeded with hMSCs. The Day 7 scaffold shows moderate levels of staining, while the Day 14 and 21 scaffolds show higher levels of Alizarin Red staining, resulting in a dark red color. Asterisks denote significance of $P < 0.05$.

The abundant porosity of the developed scaffolds is similar in total porosity and structure to those found in hydrogels composed of electrospun collagen or hyaluronic acid [51–53]. The large pore volume present in the developed silica matrix allows for more cell migration and nutrient transport into the depths of the matrix, which would result in more complete cellularization of the matrix. Also, the lack of material present in the matrix alleviates concerns about the accumulation of degradation byproducts and the cytotoxicity issues that may follow. In addition, whereas hydrogels cannot be utilized in many tissue engineering applications due to their poor mechanical properties, the developed silica matrices show competent mechanical properties that allow them to be used in mechanically demanding applications. Therefore, the developed silica matrix presents the morphological properties of hydrogels with an abundance of pore spaces, while maintaining the structural integrity of ceramic/polymer biomaterials and Bioglass.

To assess the osteogenic abilities of the silica scaffold and verify bone and osteochondral tissue engineering as one of the possible uses for the developed scaffold, basic osteogenic assessments were conducted. The alkaline phosphatase (ALP) activity of the seeded cells, which is an early marker for osteogenic differentiation, was measured to determine the commitment of the cells into the osteogenic lineage [54,55] (Fig. 8B).

hMSCs cultured on silica scaffolds showed steadily increasing ALP activity, with the largest increase in ALP activity seen between 7 and 14 days of culture. After 21 days of culture, ALP activity did not increase but remained high and comparable to that seen after 14 days of culture. On the other hand, hMSCs cultured on TCP showed significantly lower levels of ALP activity than its counterpart did after 7 and 14 days of culture. The ALP activity of the TCP control group did reach comparable levels of ALP activity after 21 days of culture. The consistently high levels of ALP activity seen for the hMSCs cultured on the silica scaffolds indicate that the cells cultured on silica underwent higher levels of osteogenic differentiation at an earlier time than the cells cultured on TCP.

To further assess osteogenic ability, hMSC-seeded silica scaffolds were subjected to *in vitro* mineralization which was quantified via Alizarin Red staining. The Alizarin Red staining of the silica scaffolds after 7, 14, and 21 days was high, reaching its maximum after 14 days of culture (Fig. 8C). Meanwhile, the cells cultured on TCP showed minimal levels of Alizarin Red staining, throughout all timepoints, indicating that very little mineralization occurred. The degree of Alizarin Red staining on the silica scaffolds was approximately 10-fold greater than that of the cells cultured on TCP throughout the timepoints, which indicates more

osteogenic differentiation of the cells cultured on silica scaffolds than cells cultured on TCP. Representative scaffolds stained with Alizarin red dye showed staining visibly increased with time in culture, reaching a dark red color by Day 21 (Fig. 8D). These results indicate that the scaffolds are capable of facilitating osteogenic differentiation of the seeded hMSCs, evidenced by the higher ALP activity and levels of cell-induced mineralization of the silica scaffold. A key factor in the enhanced osteogenic differentiation that was observed may be the inherently osteoinductive nature of amorphous silica materials. As mentioned previously, amorphous silica materials are capable of passive precipitation of calcium apatites when exposed to physiological fluids, which drives the differentiation of nearby progenitor cells into the osteogenic lineage [7–9]. This passive precipitation of calcium apatite was also noticed in this experiment on the acellular silica scaffolds that were used to normalize the cellularized silica scaffolds during Alizarin Red staining. Consequently, the precipitation of calcium apatites from the culture media, with time may have enhanced the osteogenic differentiation of the seeded hMSCs, which indicates that the developed silica scaffolds have a certain degree of osteoinductivity and may be apt for bone and osteochondral tissue engineering purposes.

4. Conclusion

In conclusion, this study reported an efficient way to synthesize amorphous silica fiber matrices as a degradable scaffold system with improved pore and mechanical properties for tissue engineering. Various matrix processing parameters including sintering temperatures and additives provide an additional degree of freedom to further manipulate pore and degradation features of this bioactive material platform with superior utility. The 90% porous matrix with 50–200 µm sized pores and allowing 500 wt% water uptake without losing structural dimensions and strength are some of the unique features of the amorphous silica matrix. This material platform presents beneficial hydrophilic properties of hydrogels and other polymeric/ceramic-based scaffold systems while minimizing the potential drawbacks of those systems such as difficulties in sterilization, handling, and rapid loss of mechanical properties due to swelling or degradation. These matrices lost 30% of the original mass in 40 weeks and supported osteogenic phenotype development of cultured hMSCs. Ongoing studies are evaluating these matrices to further enhance pore, degradation, and mechanical properties as well as biocompatibility and tissue healing ability in multiple tissue types.

CRediT authorship contribution statement

Hyun S. Kim: Conceptualization, Methodology, Investigation, Writing – original draft. **Sangamesh G. Kumbar:** Resources, Writing – review & editing, Supervision. **Syam P. Nukavarapu:** Conceptualization, Methodology, Resources, Writing – original draft, Writing – review & editing, Supervision.

Acknowledgments

The authors acknowledge support from the National Institute of Biomedical Imaging and Bioengineering (NIBIB) of the National Institutes of Health (#R01EB030060 & #R01EB020640). Dr. Nukavarapu also acknowledges funding from NSF EFMA (#1908454).

References

- [1] L.L. Hench, The story of Bioglass, *J. Mater. Sci. Mater. Med.* 17 (2006) 967–978, <https://doi.org/10.1007/s10856-006-0432-z>.
- [2] V. Krishnan, T. Lakshmi, Bioglass: a novel biocompatible innovation, *J. Adv. Pharm. Technol. Research* (JAPTR) 4 (2013) 78–83, <https://doi.org/10.4103/2231-4040.111523>.
- [3] J.R. Jones, D.S. Brauer, L. Hupa, D.C. Greenspan, Bioglass and bioactive glasses and their impact on healthcare, *Int. J. Appl. Glass Sci.* 7 (2016) 423–434, <https://doi.org/10.1111/ijag.12252>.
- [4] G. Stanciu, I. Săndulescu, B. Savu, X. Chatzistavrou, P. Koidis, Investigation of the Hydroxyapatite Growth on Bioactive Glass Surface, Undefined, 2007. <https://www.semanticscholar.org/paper/Investigation-of-the-Hydroxyapatite-Growth-on-Glass-Stanciu-S%C7%8Endulescu/9a52ef5a93cb1984e6a2c44fca84f162696d82b>. (Accessed 16 December 2021).
- [5] L.L. Hench, H.A. Paschall, Histochemical responses at a biomaterial's interface, *J. Biomed. Mater. Res.* 8 (1974) 49–64, <https://doi.org/10.1002/jbm.820080307>.
- [6] L.L. Hench, R.J. Splinter, W.C. Allen, T.K. Greenlee, Bonding mechanisms at the interface of ceramic prosthetic materials, *J. Biomed. Mater. Res.* 5 (1971) 117–141, <https://doi.org/10.1002/jbm.820050611>.
- [7] R. Hill, An alternative view of the degradation of bioglass, *J. Mater. Sci. Lett.* 15 (2016) 1122–1125, <https://doi.org/10.1007/BF00539955>.
- [8] Ö.H. Andersson, K.H. Karlsson, K. Kangasniemi, Calcium phosphate formation at the surface of bioactive glass in vivo, *J. Non-Cryst. Solids* 119 (1990) 290–296, [https://doi.org/10.1016/0022-3093\(90\)90301-2](https://doi.org/10.1016/0022-3093(90)90301-2).
- [9] K.E. Wallace, R.G. Hill, J.T. Pembroke, C.J. Brown, P.V. Hatton, Influence of sodium oxide content on bioactive glass properties, *J. Mater. Sci. Mater. Med.* 10 (1999) 697–701, <https://doi.org/10.1023/a:1008910718446>.
- [10] M. Hamadouche, A. Meunier, D.C. Greenspan, C. Blanchat, J.P. Zhong, G.P. La Torre, L. Sedel, Long-term in vivo bioactivity and degradability of bulk sol-gel bioactive glasses, *J. Biomed. Mater. Res.* 54 (2001) 560–566, [https://doi.org/10.1002/1097-4636\(20010315\)54:4<560::AID-JBM130>3.0.CO;2-J](https://doi.org/10.1002/1097-4636(20010315)54:4<560::AID-JBM130>3.0.CO;2-J).
- [11] D. Arcos, M. Vallet-Regí, Sol-gel silica-based biomaterials and bone tissue regeneration, *Acta Biomater.* 6 (2010) 2874–2888, <https://doi.org/10.1016/j.actbio.2010.02.012>.
- [12] M. Cannio, D. Bellucci, J.A. Roether, DinoN. Boccaccini, V. Cannillo, Bioactive glass applications: a literature review of human clinical trials, *Materials* 14 (2021) 5440, <https://doi.org/10.3390/ma14185440>.
- [13] C.M. Murphy, M.G. Haugh, F.J. O'Brien, The effect of mean pore size on cell attachment, proliferation and migration in collagen-glycosaminoglycan scaffolds for bone tissue engineering, *Biomaterials* 31 (2010) 461–466, <https://doi.org/10.1016/j.biomaterials.2009.09.063>.
- [14] A.R. Amini, S.P. Nukavarapu, Oxygen-tension controlled matrices for enhanced osteogenic cell survival and performance, *Ann. Biomed. Eng.* 42 (2014) 1261–1270, <https://doi.org/10.1007/s10439-014-0990-z>.
- [15] A.R. Amini, T.O. Xu, R.M. Chidambaram, S.P. Nukavarapu, Oxygen tension-controlled matrices with osteogenic and vasculogenic cells for vascularized bone regeneration in vivo, *Tissue Eng.* 22 (2016) 610–620, <https://doi.org/10.1089/ten.TEA.2015.0310>.
- [16] L.L. Hench, J.R. Jones, Bioactive glasses: frontiers and challenges, *Front. Bioeng. Biotechnol.* 3 (2015), <https://doi.org/10.3389/fbioe.2015.00194>.
- [17] K.S. Finnie, D.J. Waller, F.L. Perret, A.M. Krause-Heuer, H.Q. Lin, J.V. Hanna, C. J. Barbe, Biodegradability of sol-gel silica microparticles for drug delivery, *J. Sol. Gel Sci. Technol.* 49 (2009) 12–18, <https://doi.org/10.1007/s10971-008-1847-4>.
- [18] S. Prabha, D. Durgalakshmi, P. Aruna, S. Ganesan, Influence of the parameters in the preparation of silica nanoparticles from biomass and chemical silica precursors towards bioimaging application, *Vacuum* 160 (2019) 181–188, <https://doi.org/10.1016/j.vacuum.2018.11.030>.
- [19] B.G. Cha, J. Kim, Functional mesoporous silica nanoparticles for bio-imaging applications, *WIREs Nanomed. Nanobiotechnol.* 11 (2019), e1515, <https://doi.org/10.1002/wnan.1515>.
- [20] D.L. Dorcenus, E.O. George, C.N. Dealy, S.P. Nukavarapu, Harnessing external cues: development and evaluation of an in vitro culture system for osteochondral tissue engineering, *Tissue Eng.* 23 (2017) 719–737, <https://doi.org/10.1089/ten.tea.2016.0439>.
- [21] D.L. Dorcenus, H.S. Kim, S.P. Nukavarapu, Gradient scaffold with spatial growth factor profile for osteochondral interface engineering, *Biomed. Mater. Bristol Engl.* (2020), <https://doi.org/10.1088/1748-605X/abd1ba>.
- [22] J.J. Blaker, S.N. Nazhat, V. Maquet, A.R. Boccaccini, Long-term in vitro degradation of PDLA/Bioglass® bone scaffolds in acellular simulated body fluid, *Acta Biomater.* 7 (2011) 829–840, <https://doi.org/10.1016/j.actbio.2010.09.013>.
- [23] A.R. Boccaccini, V. Maquet, Bioresorbable and bioactive polymer/Bioglass® composites with tailored pore structure for tissue engineering applications, *Compos. Sci. Technol.* 63 (2003) 2417–2429, [https://doi.org/10.1016/S0266-3538\(03\)00275-6](https://doi.org/10.1016/S0266-3538(03)00275-6).
- [24] G. Vergnol, N. Ginsac, P. Rivory, S. Meille, J.-M. Chenal, S. Balvay, J. Chevalier, D. J. Hartmann, In vitro and in vivo evaluation of a poly(lactic acid)-bioactive glass composite for bone fixation devices, *J. Biomed. Mater. Res. B Appl. Biomater.* 104 (2016) 180–191, <https://doi.org/10.1002/jbm.b.33364>.
- [25] M. Barbeck, T. Serra, P. Booms, S. Stojanovic, S. Najman, E. Engel, R. Sader, C. J. Kirkpatrick, M. Navarro, S. Ghanaati, Analysis of the in vitro degradation and the in vivo tissue response to bi-layered 3D-printed scaffolds combining PLA and biphasic PLA/bioglass components – guidance of the inflammatory response as basis for osteochondral regeneration, *Bioact. Mater.* 2 (2017) 208–223, <https://doi.org/10.1016/j.bioactmat.2017.06.001>.
- [26] K. Kolan, Y. Liu, J. Baldrige, C. Murphy, J. Semon, D. Day, M. Leu, Solvent based 3D printing of biopolymer/bioactive glass composite and hydrogel for tissue engineering applications, *Procedia CIRP* 65 (2017) 38–43, <https://doi.org/10.1016/j.procir.2017.04.022>.
- [27] C.G. Pitt, M.M. Gratzl, G.L. Kimmel, J. Surlis, A. Schindler, Aliphatic polyesters II. The degradation of poly (DL-lactide), poly (epsilon-caprolactone), and their copolymers in vivo, *Biomaterials* 2 (1981) 215–220.

- [28] K. Fu, D.W. Pack, A.M. Klibanov, R. Langer, Visual evidence of acidic environment within degrading poly(lactic-co-glycolic acid) (PLGA) microspheres, *Pharm. Res. (N. Y.)* 17 (2000) 100–106, <https://doi.org/10.1023/A:1007582911958>.
- [29] A.R. Amini, J.S. Wallace, S.P. Nukavarapu, Short-term and long-term effects of orthopedic biodegradable implants, *J. Long Term Eff. Med. Implants* 21 (2011) 93–122.
- [30] J.M. Anderson, M.S. Shive, Biodegradation and biocompatibility of PLA and PLGA microspheres, *Adv. Drug Deliv. Rev.* 64 (2012) 72–82, <https://doi.org/10.1016/j.addr.2012.09.004>.
- [31] S.G. Lévesque, R.M. Lim, M.S. Shoichet, Macroporous interconnected dextran scaffolds of controlled porosity for tissue-engineering applications, *Biomaterials* 26 (2005) 7436–7446, <https://doi.org/10.1016/j.biomaterials.2005.05.054>.
- [32] X. Shi, B. Sitharaman, Q.P. Pham, F. Liang, K. Wu, W. Edward Billups, L.J. Wilson, A.G. Mikos, Fabrication of porous ultra-short single-walled carbon nanotube nanocomposite scaffolds for bone tissue engineering, *Biomaterials* 28 (2007) 4078–4090, <https://doi.org/10.1016/j.biomaterials.2007.05.033>.
- [33] ASTM D695-15, Standard Test Method for Compressive Properties of Rigid Plastics, ASTM International, West Conshohocken, PA, 2012. <https://www.astm.org/Standards/D695.htm>.
- [34] D.W.L. Hukins, A. Mahomed, S.N. Kukureka, Accelerated aging for testing polymeric biomaterials and medical devices, *Med. Eng. Phys.* 30 (2008) 1270–1274, <https://doi.org/10.1016/j.medengphy.2008.06.001>.
- [35] T.O. Xu, H.S. Kim, T. Stahl, S.P. Nukavarapu, Self-neutralizing PLGA/magnesium composites as novel biomaterials for tissue engineering, *Biomed. Mater. Bristol Engl.* 13 (2018), 035013, <https://doi.org/10.1088/1748-605X/aaa29>.
- [36] P.E. Mikael, A.A. Golebiowska, S.G. Kumbar, S.P. Nukavarapu, Evaluation of autologously derived biomaterials and stem cells for bone tissue engineering, *Tissue Eng.* 26 (2020) 1052–1063, <https://doi.org/10.1089/ten.TEA.2020.0011>.
- [37] S. Tanaka, C.C. Pin, K. Uematsu, Effect of organic binder segregation on sintered strength of dry-pressed alumina, *J. Am. Ceram. Soc.* 89 (2006) 1903–1907, <https://doi.org/10.1111/j.1551-2916.2006.01057.x>.
- [38] H.-H. Tang, M.-L. Chiu, H.-C. Yen, Slurry-based selective laser sintering of polymer-coated ceramic powders to fabricate high strength alumina parts, *J. Eur. Ceram. Soc.* 31 (2011) 1383–1388, <https://doi.org/10.1016/j.jeurceramsoc.2011.02.020>.
- [39] R. Taktak, S. Baklouti, J. Bouaziz, Effect of binders on microstructural and mechanical properties of sintered alumina, *Mater. Char.* 62 (2011) 912–916, <https://doi.org/10.1016/j.matchar.2011.06.011>.
- [40] H. Yang, S. Xu, L. Jiang, Y. Dan, Thermal decomposition behavior of poly(vinyl alcohol) with different hydroxyl content, *J. Macromol. Sci. Part B* 51 (2012) 464–480, <https://doi.org/10.1080/00222348.2011.597687>.
- [41] M.T. Taghizadeh, N. Yeganeh, M. Rezaei, The investigation of thermal decomposition pathway and products of poly(vinyl alcohol) by TG-FTIR, *J. Appl. Polym. Sci.* 132 (2015), <https://doi.org/10.1002/app.42117>.
- [42] S. Soares, G. Camino, S. Levchik, Comparative study of the thermal decomposition of pure cellulose and pulp paper, *Polym. Degrad. Stabil.* 49 (1995) 275–283, [https://doi.org/10.1016/0141-3910\(95\)87009-1](https://doi.org/10.1016/0141-3910(95)87009-1).
- [43] D.K. Shen, S. Gu, The mechanism for thermal decomposition of cellulose and its main products, *Bioresour. Technol.* 100 (2009) 6496–6504, <https://doi.org/10.1016/j.biortech.2009.06.095>.
- [44] H.K. Makadia, S.J. Siegel, Poly lactic-co-glycolic acid (PLGA) as biodegradable controlled drug delivery carrier, *Polymers* 3 (2011) 1377–1397, <https://doi.org/10.3390/polym3031377>.
- [45] N.V. Gupta, H.G. Shivakumar, Investigation of swelling behavior and mechanical properties of a pH-sensitive superporous hydrogel composite, *Iran, J. Pharm. Res. IJPR* 11 (2012) 481–493.
- [46] Q. Chai, Y. Jiao, X. Yu, Hydrogels for biomedical applications: their characteristics and the mechanisms behind them, *Gels* 3 (2017) 6, <https://doi.org/10.3390/gels3010006>.
- [47] H. Kamata, X. Li, U. Chung, T. Sakai, Design of hydrogels for biomedical applications, *Adv. Healthc. Mater.* 4 (2015) 2360–2374, <https://doi.org/10.1002/adhm.201500076>.
- [48] E.A. Vogler, Structure and reactivity of water at biomaterial surfaces, *Adv. Colloid Interface Sci.* 74 (1998) 69–117, [https://doi.org/10.1016/S0001-8686\(97\)00040-7](https://doi.org/10.1016/S0001-8686(97)00040-7).
- [49] I.D. Xynos, A.J. Edgar, L.D.K. Buttery, L.L. Hench, J.M. Polak, Ionic products of bioactive glass dissolution increase proliferation of human osteoblasts and induce insulin-like growth factor II mRNA expression and protein synthesis, *Biochem. Biophys. Res. Commun.* 276 (2000) 461–465, <https://doi.org/10.1006/bbrc.2000.3503>.
- [50] I.D. Xynos, A.J. Edgar, L.D.K. Buttery, L.L. Hench, J.M. Polak, Gene-expression profiling of human osteoblasts following treatment with the ionic products of Bioglass® 45S5 dissolution, *J. Biomed. Mater. Res.* 55 (2001) 151–157, [https://doi.org/10.1002/1097-4636\(200105\)55:2<151::AID-JBM1001>3.0.CO;2-D](https://doi.org/10.1002/1097-4636(200105)55:2<151::AID-JBM1001>3.0.CO;2-D).
- [51] Y. Wakuda, S. Nishimoto, S. Suye, S. Fujita, Native collagen hydrogel nanofibers with anisotropic structure using core-shell electrospinning, *Sci. Rep.* 8 (2018) 6248, <https://doi.org/10.1038/s41598-018-24700-9>.
- [52] Y. Ji, K. Ghosh, B. Li, J.C. Sokolov, R.A.F. Clark, M.H. Rafailovich, Dual-syringe reactive electrospinning of cross-linked hyaluronic acid hydrogel nanofibers for tissue engineering applications, *Macromol. Biosci.* 6 (2006) 811–817, <https://doi.org/10.1002/mabi.200600132>.
- [53] I.L. Kim, S. Khetan, B.M. Baker, C.S. Chen, J.A. Burdick, Fibrous hyaluronic acid hydrogels that direct MSC chondrogenesis through mechanical and adhesive cues, *Biomaterials* 34 (2013) 5571–5580, <https://doi.org/10.1016/j.biomaterials.2013.04.004>.
- [54] E.E. Golub, K. Boesze-Battaglia, The role of alkaline phosphatase in mineralization, *Curr. Opin. Orthop.* 18 (2007) 444–448, <https://doi.org/10.1097/BCO.0b013e3282630851>.
- [55] T. Nakamura, A. Nakamura-Takahashi, M. Kasahara, A. Yamaguchi, T. Azuma, Tissue-nonspecific alkaline phosphatase promotes the osteogenic differentiation of osteoprogenitor cells, *Biochem. Biophys. Res. Commun.* 524 (2020) 702–709, <https://doi.org/10.1016/j.bbrc.2020.01.136>.
- [56] X. Liu, P.X. Ma, Polymeric scaffolds for bone tissue engineering, *Ann. Biomed. Eng.* 32 (2004) 477–486.
- [57] J. Jeong, J.H. Kim, J.H. Shim, N.S. Hwang, C.Y. Heo, Bioactive calcium phosphate materials and applications in bone regeneration, *Biomater. Res.* 23 (2019) 4, <https://doi.org/10.1186/s40824-018-0149-3>.
- [58] N. Annabi, J.W. Nichol, X. Zhong, C. Ji, S. Koshy, A. Khademhosseini, F. Dehghani, Controlling the porosity and microarchitecture of hydrogels for tissue engineering, *Tissue Eng. B Rev.* 16 (2010) 371–383, <https://doi.org/10.1089/ten.teb.2009.0639>.
- [59] V. Keskar, N.W. Marion, J.J. Mao, R.A. Gemeinhart, In vitro evaluation of macroporous hydrogels to facilitate stem cell infiltration, growth, and mineralization, *Tissue Eng.* 15 (2009) 1695–1707, <https://doi.org/10.1089/ten.tea.2008.0238>.
- [60] X. Zhang, Y. Li, D. He, Z. Ma, K. Liu, K. Xue, H. Li, An effective strategy for preparing macroporous and self-healing bioactive hydrogels for cell delivery and wound healing, *Chem. Eng. J.* 425 (2021), 130677, <https://doi.org/10.1016/j.cej.2021.130677>.
- [61] D.M.R. Gibbs, C.R.M. Black, J.I. Dawson, R.O.C. Oreffo, A review of hydrogel use in fracture healing and bone regeneration, *J. Tissue Eng. Regen. Med.* 10 (2016) 187–198, <https://doi.org/10.1002/term.1968>.
- [62] S. Li, Hydrolytic degradation characteristics of aliphatic polyesters derived from lactic and glycolic acids, *J. Biomed. Mater. Res.* 48 (1999) 342–353, [https://doi.org/10.1002/\(SICI\)1097-4636\(1999\)48:3<342::AID-JBM20>3.0.CO;2-7](https://doi.org/10.1002/(SICI)1097-4636(1999)48:3<342::AID-JBM20>3.0.CO;2-7).
- [63] L.N. Woodard, M.A. Grunlan, Hydrolytic degradation and erosion of polyester biomaterials, *ACS Macro Lett.* 7 (2018) 976–982, <https://doi.org/10.1021/acsmacrolett.8b00424>.
- [64] R. Galante, T.J.A. Pinto, R. Colaço, A.P. Serro, Sterilization of hydrogels for biomedical applications: a review, *J. Biomed. Mater. Res. B Appl. Biomater.* 106 (2018) 2472–2492, <https://doi.org/10.1002/jbm.b.34048>.